Check for updates

ADVANCED FUNCTIONAL MATERIALS
www.afm-journal.de

Revealing the Active Sites in Atomically Dispersed Multi-Metal–Nitrogen–Carbon Catalysts

Buwei Sun, Shiyu Zhang, Haozhou Yang, Tianyu Zhang, Qiujiang Dong, Wanxing Zhang, Jia Ding, Xiaogang Liu, Lei Wang, Xiaopeng Han,* and Wenbin Hu**

Atomically dispersed metal-nitrogen-carbon catalysts have been extensively explored for various sustainable energy-related reactions. From a material perspective, these catalysts are likely to consist of a combination of single-atom, dual-atom and possibly even multi-atom sites. However, pinpointing their true active sites has remained a challenging task. In this study, a model catalyst is introduced, Co/CoMn-NC, featuring both Co single-atom sites and CoMn dual-atom sites on a nitrogen-doped carbon substrate. By employing a combination of X-ray adsorption spectroscopy and density functional theory calculations, the atomic configuration of Co/CoMn-NC has been determined. Density functional theory calculations are also used to unequivocally identify Co-atom within the CoMn dual-atom motif as the predominate active site of the Co/CoMn-NC model catalyst toward oxygen reduction reaction (ORR), which is further confirmed by in situ Raman spectroscopy. The cooperative interactions between Co single-atom sites and CoMn dual-atom sites can finely tune the d-band center and ameliorate the adsorption and desorption behaviors of the intermediates, thereby facilitating ORR kinetic. Overall, the study introduces a systematic strategy to elucidate the structure and the superiority of the model system and provides new insights into atomically dispersed multi-metal active sites, showcasing that enhanced catalytic performance extends beyond unified diatomic sites or monatomic sites.

1. Introduction

Recently, single-atom catalysts (SACs) with high atom utilization and unique electronic features have received immense scientific interest in various catalytic fields such as electrocatalysis,[1–3] photocatalysis,[4–6] and organic catalysis.[7–9] The majority of SACs consist of isolated single metal sites coordinated with the neighboring nitrogen atoms in carbon matrix (M-NC).[10–12] The unsaturated coordination effect and quantum size effect make single-atom catalysts usually have better catalytic activity in many reactions. Meanwhile, the uniform reaction sites greatly enhance the selectivity of specific reactions. There are various types of catalytic reactions involved in single atom, mainly including CO oxidation and selective oxidation, hydrogenation and selective hydrogenation, NO reduction and oxidation, water gas conversion, organic synthesis, methanol steam reforming, fuel cells, photoelectric catalysis, formaldehyde oxidation, etc.[13–15] However, this configuration poses challenges in achieving superior catalytic activity/selectivity for complicated reactions involving multiple reaction steps and intermediates, as they are exposed to only one specific type of active site.[16–18] Meanwhile, to preserve the single-atom configuration, the metal loading is often restricted to prevent aggregation.[19,20] In response to this, recent exploration has reported that dual-atom catalysts (DACs), as an extension of SACs, have the potential to enhance the intrinsic activity of active centers in various conversion reactions. This is attributed to the unique atomic interface and synergistic effects of the dual-metal sites.[21–24] Dual-atomic sites also offer a greater number of available active sites, which allows for increased loading of metal atoms.[25–27] Owning to these advantages, significant efforts have been dedicated to the development of the DACs for various of catalytic applications, such as Fe–Co dual-metal single atoms in the oxygen reduction

B. Sun, X. Liu, W. Hu
Joint School of National University of Singapore and Tianjin University
International Campus of Tianjin University
Binhai New City, Fuzhou 350207, P. R. China
E-mail: wbhu@tju.edu.cn

B. Sun, X. Liu
Department of Chemistry
National University of Singapore
Singapore 117543, Singapore

The ORCID identification number(s) for the author(s) of this article can be found under https://doi.org/10.1002/adfm.202315862

DOI: 10.1002/adfm.202315862

S. Zhang, Q. Dong, W. Zhang, J. Ding, X. Han, W. Hu
School of Materials Science and Engineering
Key Laboratory of Advanced Ceramics and Machining Technology of Ministry of Education
Tianjin University
Tianjin 300072, P. R. China
E-mail: xphan@tju.edu.cn

H. Yang, T. Zhang, L. Wang
Department of Chemical and Biomolecular Engineering
National University of Singapore
Singapore 117585, Singapore
E-mail: wanglei8@nus.edu.sg

 © 2024 Wiley-VCH GmbH

reaction (ORR),[28] NiCo single-atom dimer in the hydrogen evolution reaction (HER),[29] Fe-Mo diatomic catalytic pair in the CO_2 reduction reaction (CO_2RR)[30] and Pd-Cu dual-atom catalyst in the low-temperature acetylene semi-hydrogenation.[31]

Structurally, many dual-atom catalysts do not exhibit an ideal distribution of the two metal active sites. High-angle annular dark-field imaging from scanning transmission electron microscopes (HAADF-STEM) often reveals the presence of single, dual and even multiple atom sites.[32–36] Likewise, the presence of non-negligible diatomic pairs also occurs in single-atom catalyst systems.[8,37–40] Therefore, we believe that the coexistence of single atomic and diatomic sites, and potentially more complex configurations, is a common occurrence, however, the synergies among these different types of sites and their actual functions during the catalytic processes have been overlooked. Clarifying the true active center and the underlying catalytic mechanism holds significant importance for single/dual-atom catalytic systems across various fields. In this study, we introduce a systematic strategy to elucidate the structure of a model system comprising various types of active sites and to further understand their functions in a typical energy-related oxygen reduction reaction.

In this work, we constructed a model catalyst consisting of Co single-atom sites and CoMn dual-atom sites on N-doped carbon substrate (Co/CoMn-NC) and demonstrated an effective strategy in revealing its true catalytic active-site for oxygen reduction reaction (ORR). Specifically, we first introduced the CoMn diatomic sites through the pyrolysis of CoZn-zeolitic imidazolate framework (ZIF-8) precursor with adsorption of Mn salt at high temperature. To prove that the introduced Mn-sites are more inclined to form CoMn diatomic structure with Co-sites, we calculated the binding energies of different structures for Mn (Figure S1, Supporting Information), as shown in Figure S2 (Supporting Information). It became evident that the N_4 structure exhibits a stronger binding energy to Co than Mn, making it challenging for Mn species to maintain the conventional Mn-N_4 structure. Subsequently, we calculated the binding energies of four structural models, revealing that the direct bonding structure between Co and Mn is more conducive to Mn bonding and forms a stable diatomic structure. To validate the atomic structure of the Co/CoMn-NC catalyst constructed through density functional theory (DFT) calculations, we employed X-ray absorption near-edge structure (XANES) spectroscopy and extended X-ray absorption fine structure (EXAFS) spectroscopy. We then evaluated the catalytic activity of Co/CoMn-NC using ORR as a model reaction. The synergy of Co single-atom sites and CoMn dual-atom sites significantly enhances the ORR performance of Co/CoMn-NC under alkaline conditions with a half-wave potential ($E_{1/2}$) of 0.89 V. This outperforms Co-NC (0.81 V), CoMnNC (0.85 V), and even the commercial Pt/C catalyst (0.87 V). Furthermore, the Zn–air battery performance of Co/CoMn-NC, with a power density of 213 mW cm^{-2} at 401 mA cm^{-2}, also surpasses that of Pt/C, which achieves 136 mW cm^{-2} at 258 mA cm^{-2}. Building upon our robust understanding of the atomic structure of Co/CoMn-NC, as discussed earlier, we combined in situ Raman spectroscopy with DFT calculations. This allowed us to identify that the Co site within the CoMn dual-atom site is the predominant active center in the Co/CoMn-NC catalysts. The interaction between Co single-atom sites and CoMn dual-atom sites optimizes the electronic structure of these active centers, including Co single-atom sites and Co site within the CoMn dual-atom sites, enhancing the adsorption and desorption behaviors of key reaction intermediates, thereby significantly improving ORR kinetics.

2. Results and Discussion

The synthetic strategy for Co/CoMn-NC is schematically illustrated in **Figure 1a**. Typically, the CoZn–ZIF precursor was first self-assembled by Co^{2+}, Zn^{2+}, and 2-methylimidazole ligand, which was then utilized to introduce Mn sites into the nanocages of ZIF-8. Subsequently, after annealing at 950 °C in argon, the precursor was then pyrolyzed to afford Co/CoMn-NC on the N-doped carbon matrix. The weight percentages of Co, Mn were determined as 1.75 and 0.82 wt.% respectively, using inductively coupled plasma mass spectrometry (ICP-MS) (Table S1, Supporting Information). The single metal atomically dispersed Co-NC, Mn-NC, and CoMn-NC with different ratio of Co/Mn obtained through a similar process were also synthesized as controlled samples. As shown in Figure S3 (Supporting Information), the X-ray diffraction (XRD) patterns show no characteristic crystal peaks for metal, metal nitride and metal carbide within Co-NC, Mn-NC, and CoMn-NC with different Co/Mn ratio (1:1 as CoMn-NC, 2:1 as Co/CoMn-NC, 4:1, 8:1). The result excludes the formation of large metallic particles in the above samples. The scanning electron microscopy (SEM) images show that the samples are rhomboid dodecahedron with an average size of ≈300 nm (Figure S4, Supporting Information). Notably, the introduction of Mn causes a significant morphological irregularity whereas no obvious size changes occurred. Meanwhile, Brunauer–Emmett–Teller (BET) values of the catalysts show that the introduction of Mn will drastically reduces the specific surface area of the catalyst caused by the adsorption of Mn blocking the pores of ZIF-8 (Figure S5, Supporting Information). Transmission electron microscopy (TEM) images further reveal that Co/CoMn-NC is composed of amorphous carbon, and no obvious metal nanoparticles could be spotted, demonstrating that both Co and Mn are mostly dispersed in the Co/CoMn-NC atomically (Figure S6, Supporting Information).[41] HAADF-STEM was employed to characterize the state of Co atoms and Co-Mn dual-sites in the catalyst. HAADF-STEM image in Figure 1c demonstrates the existence of Co-Mn dual-sites (marked by the red circle) along with some isolated Co atoms (marked by the yellow circle). Electron energy-loss spectroscopy (EELS) was used to identify the real existence of Co-Mn dual sites in Co/CoMn-NC according to the intensity profile and corresponding electron energy loss (Figure 1d).[42] Statistical analysis of multiple dimer sites, as shown in Figure 1e,f, indicates that the distance between Co-Mn dual-sites is ≈0.24 ± 0.02 nm. Energy-dispersive X-ray spectroscopic (EDS) elemental mapping confirmes the homogeneous distribution of Co, Mn, N, and C atoms in the Co/CoMn-NC. Additionally, the chemical composition of Co/CoMn-NC was further investigated using X-ray photoelectron spectroscopy (XPS). Furthermore, the C 1s XPS spectrum of Co/CoMn-NC is shown in Figure S11a (Supporting Information), where three peaks are observed and can be attributed to C═C, C─N/C═N, and C═O, respectively. Besides, as illustrated in Figure S11b (Supporting Information), the N 1s spectrum of Co/CoMn-NC reveals five distinct N species, including oxidized N, graphitic N, pyrrolic N, metal-N species,

© 2024 Wiley-VCH GmbH

16163028, 0, Downloaded from https://onlinelibrary.wiley.com/doi/10.1002/adfm.202315862 by National University Of Singapore Nus Libraries, Wiley Online Library on [24/04/2024]. See the Terms and Conditions (https://onlinelibrary.wiley.com/terms-and-conditions) on Wiley Online Library for rules of use; OA articles are governed by the applicable Creative Commons License

16163028, 0, Downloaded from https://onlinelibrary.wiley.com/doi/10.1002/adfm.202315862 by National University Of Singapore Nus Libraries, Wiley Online Library on [24/04/2024]. See the Terms and Conditions (https://onlinelibrary.wiley.com/terms-and-conditions) on Wiley Online Library for rules of use; OA articles are governed by the applicable Creative Commons License

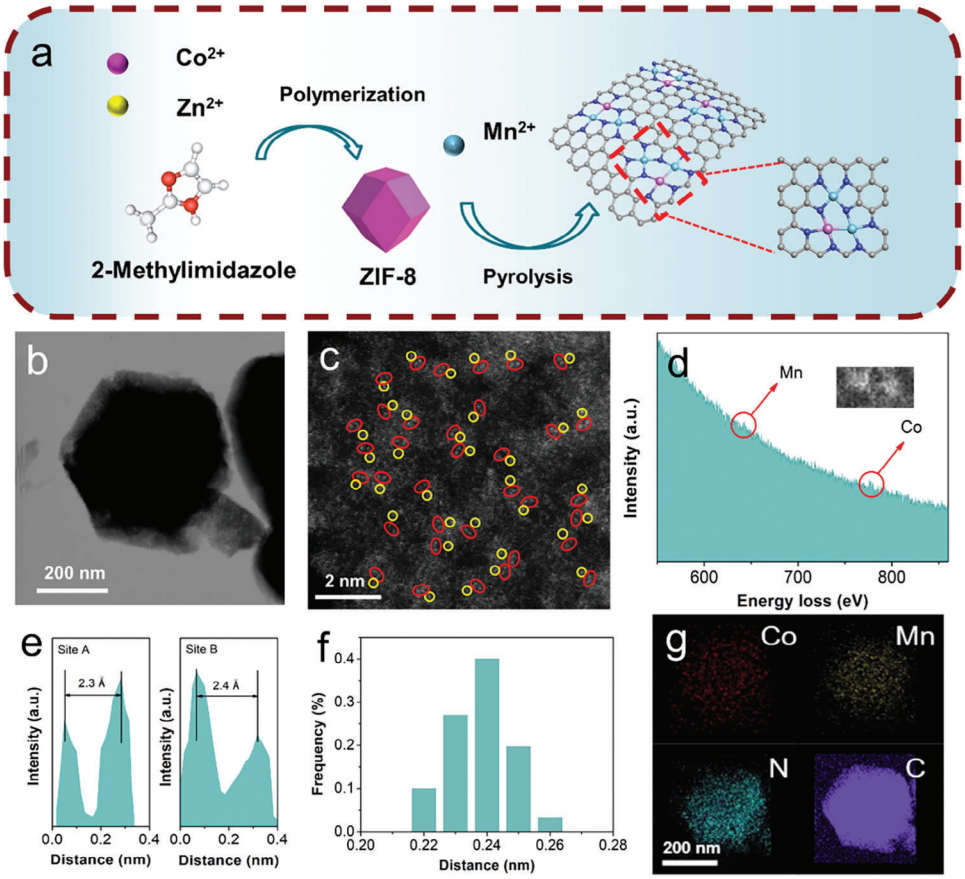

Figure 1. Synthetic strategy and structural analysis of Co/CoMn-NC. a) Schematic illustration of the synthetic procedure for Co/CoMn-NC. b) TEM images of Co/CoMn-NC. c) Aberration-corrected HAADF-STEM image of Co/CoMn-NC. Co-Mn dual-sites are marked by the red circle along with some isolated Co atoms marked by the yellow circle. d) Co/CoMn-NC structure analyzed by EELS. e) The intensity profiles obtained on two bimetallic Co–Mn sites. f) Statistical Co–Mn distance in the observed diatomic pairs. g) HAADF-STEM image of Co/CoMn-NC with mappings of individual elements (Co, Mn, N, and C).

and pyridinic N. Lastly, the Raman spectra of Co/CoMn-NC reveal an intensity ratio (I_D/I_G) of ≈1.13 for the two broad peaks at ≈1352 and 1583 cm^{-1} (see Figure S12 and Table S2, Supporting Information). The higher I_D/I_G ratio in the Raman spectra indicates the generation of more defects in Co/CoMn-NC. These defects are beneficial as they expose more catalytically active sites, thus enhancing catalytic activity.[43]

The local electronic structures of Co and Mn in Co/CoMn-NC were further investigated using XANES and EXAFS measurements. Co K-edge XANES spectra (**Figure** 2a) show that the Co K-pre-edges of both Co-NC and Co/CoMn-NC lie between those of CoO and Co_3O_4. Specifically, the Co K-pre-edge of Co/CoMn-NC closely resembles that of CoO, indicating a lower oxidation state of Co in Co/CoMn-NC compared to Co-NC. This suggests electron transfer from Mn to Co. Co K-edge FT-EXAFS spectra reveal that the main peak at ≈1.56 Å corresponds to the Co-N scattering path, rather than the Co—Co bond (see Figure 2b), confirming that the Co atoms in both Co-NC and Co/CoMn-NC are atomically dispersed. Notably, a notable secondary peak emerges at a larger distance of 2.40 Å in the Co/CoMn-NC sample, which is absent in Co-NC. This presence suggests the existence of a Co-Mn dual-sites. Moreover, as shown in Figure 2c, the Mn K-pre-edges of Co/CoMn-NC lie between those of MnO and MnO_2, indicating that the valence states of Mn in Co/CoMn-NC are positive and situated between +2 and +4. Similarly, as shown in Figure 2d, the FT-EXAFS spectra of Mn K-edge demonstrate that Co/CoMn-NC shows a peak at 1.40 Å indexing Mn–N coordination, and a peak at 2.40 Å, consistent with the FT-EXAFS spectra of the Co K-edge. Additionally, the wavelet transform (WT) contour plots at the Co K-edge of Co/CoMn-NC show a high intensity at ≈4.4 $Å^{-1}$ (Figure 2e), corresponding to Co-N coordination in Co/CoMn-NC. Moreover, another intensity peak with a *k* value of ≈6.8 $Å^{-1}$ was observed in Co/CoMn-NC, indicating the formation of Co—Mn bond. Similar conclusions can be made from the WT analysis of the Mn K-edge for Co/CoMn-NC. The fitting results in R and k space (Figure 2f,g; Table S4, Supporting Information) indicate that the coordination numbers of Co–N_1, Co–N_2, Co–N_3, Co-Mn, and Co–Co are 3.9, 2.0, 1.0, 1.0, and 1.0, respectively, and the coordination numbers of Mn–N_1, Mn–N_2, Mn–Co_1 and Mn–Co_2 are 2.0, 1.0, 1.0, and 1.0, respectively. Taken together, the model structure as depicted in Figure 2f inset is considered to be the most likely structure for Co/CoMn-NC. To further validate this atomic configuration of Co/CoMn-NC, DFT was utilized to deduce the most reasonable structure of Co/CoMn-NC

 © 2024 Wiley-VCH GmbH

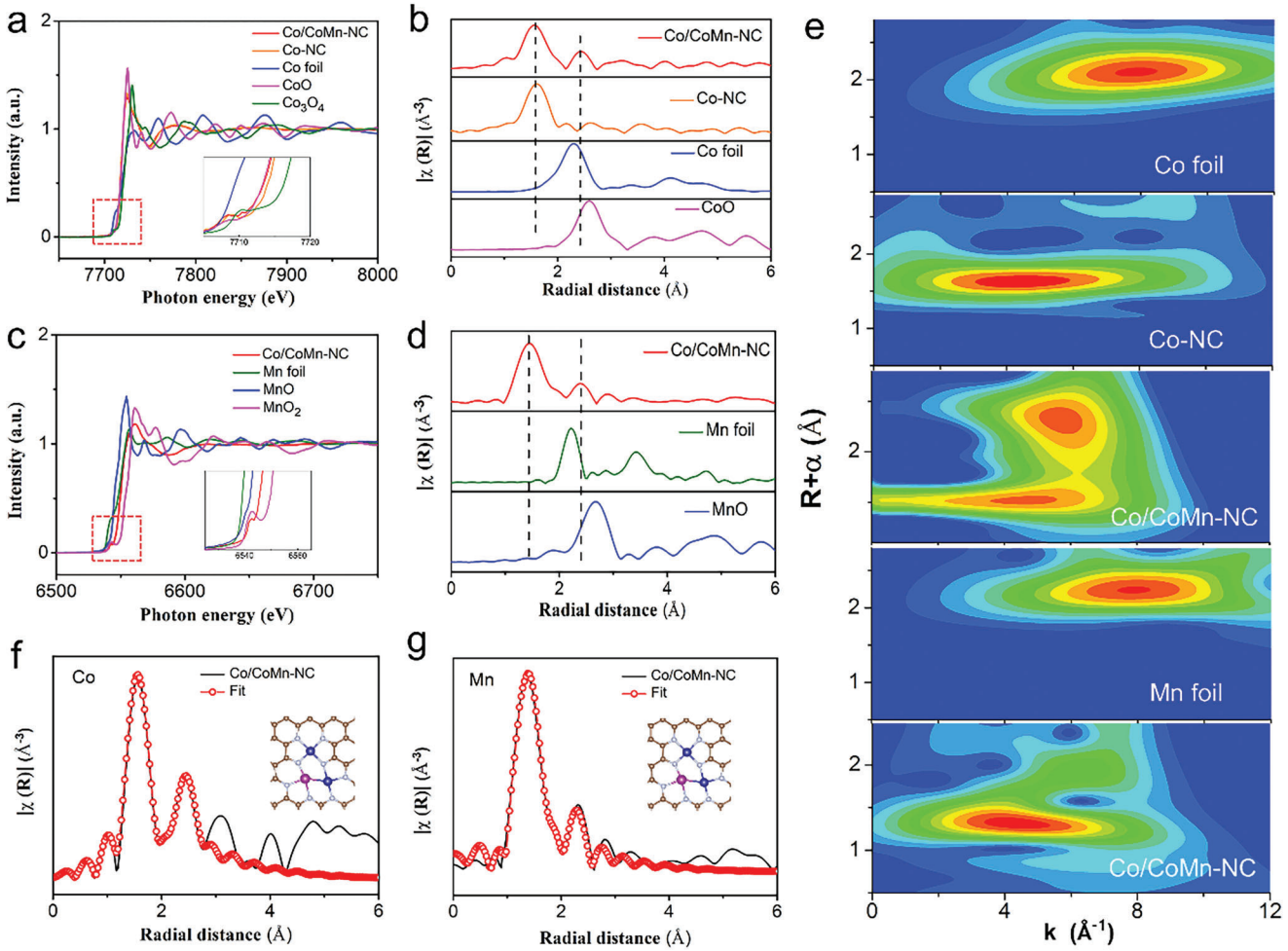

Figure 2. Electronic structural characterization of Co/CoMn-NC catalysts by XAS. a) Co K-edge XANES and b) Fourier-transform EXAFS spectra of Co/CoMn-NC and reference samples. c) Mn K-edge XANES and d) Fourier-transform EXAFS spectra of Co/CoMn-NC and reference samples. e) WT-EXAFS spectra of Co/CoMn-NC along with reference samples. f,g) FT-EXAFS fitting curves of Co and Mn K-edge for Co/CoMn-NC (inset: structural model of Co/CoMn-NC).

(Figure S13, Supporting Information) by comparing the experimental and theoretical spectra of K-edge EXAFS. Based on the simulated Co K-edge spectra of EXAFS, the calculated Co/CoMn-NC model shown in Figure S13a (Supporting Information) agrees well with experimental spectra. In contrast, other proposed structural models could be excluded (Figure S14, Supporting Information). In addition, the formation energy of the model structure showing in Figure S13a (Supporting Information) (−4.33eV) is the lowest among all structural models, indicating its superior energetic stability. Compared with previously reported dual-metal centers in M–N–C structures,[23,29,44–49] Co/CoMn-NC adopts a novel synergistic coordination configuration of Co single-atom sites and CoMn dual-atom sites.

The ORR performance of Co-NC, Mn-NC, Pt/C (20 wt.%) and CoMn-NC with different Co/Mn ratios were first evaluated using cyclic voltammetry (CV) and linear scan voltammetry (LSV) in a rotating ring-disk electrode (RRDE) system in O_2-saturated 0.1 M KOH electrolyte. CV curves for different samples are shown in Figure S15 (Supporting Information), revealing a more positive position of the oxygen reduction peak and higher current density for Co/CoMn-NC, indicating a higher electrocatalytic ORR activity. LSV curves were measured for the different samples in O_2-saturated 0.1 M KOH solution at different rotation rates (Figure S16, Supporting Information). As shown in **Figure 3a**, compared with Co-NC, Co Mn-NC, and commercial Pt/C, the well-defined Co/CoMn-NC catalyst has improved ORR activity with an $E_{1/2}$ of 0.89 V versus RHE and a calculated kinetic current density (J_k) of 15.1 mA cm^{-2} at 0.85 V versus RHE (Figure 3b). This notable ORR performance of Co/CoMn-NC surpasses most of the non-noble catalysts reported and is also higher than the commercial Pt/C under the same testing conditions (Table S4, Supporting Information). Meanwhile, Co/CoMn-NC exhibits the smallest Tafel slope of 56 mV dec^{-1}, indicating that the Co/CoMn-NC has the fastest ORR kinetics (Figure 3c). The Tafel slope of ORR on Co/CoMn-NC also suggests that the rate-determining step is shifted to the desorption of OH*.[50,51] The electron transfer number (n) of 3.9 and the H_2O_2 yield of below 5% were evaluated through RRDE over the potential range of 0.3–0.8 V, certifying the high 4e$^-$ selectivity of Co/CoMn-NC for ORR (Figure 3d). The apparent 4e$^-$ pathway is also

© 2024 Wiley-VCH GmbH

16163028, 0, Downloaded from https://onlinelibrary.wiley.com/doi/10.1002/adfm.202315862 by National University Of Singapore Nus Libraries, Wiley Online Library on [24/04/2024]. See the Terms and Conditions (https://onlinelibrary.wiley.com/terms-and-conditions) on Wiley Online Library for rules of use; OA articles are governed by the applicable Creative Commons License

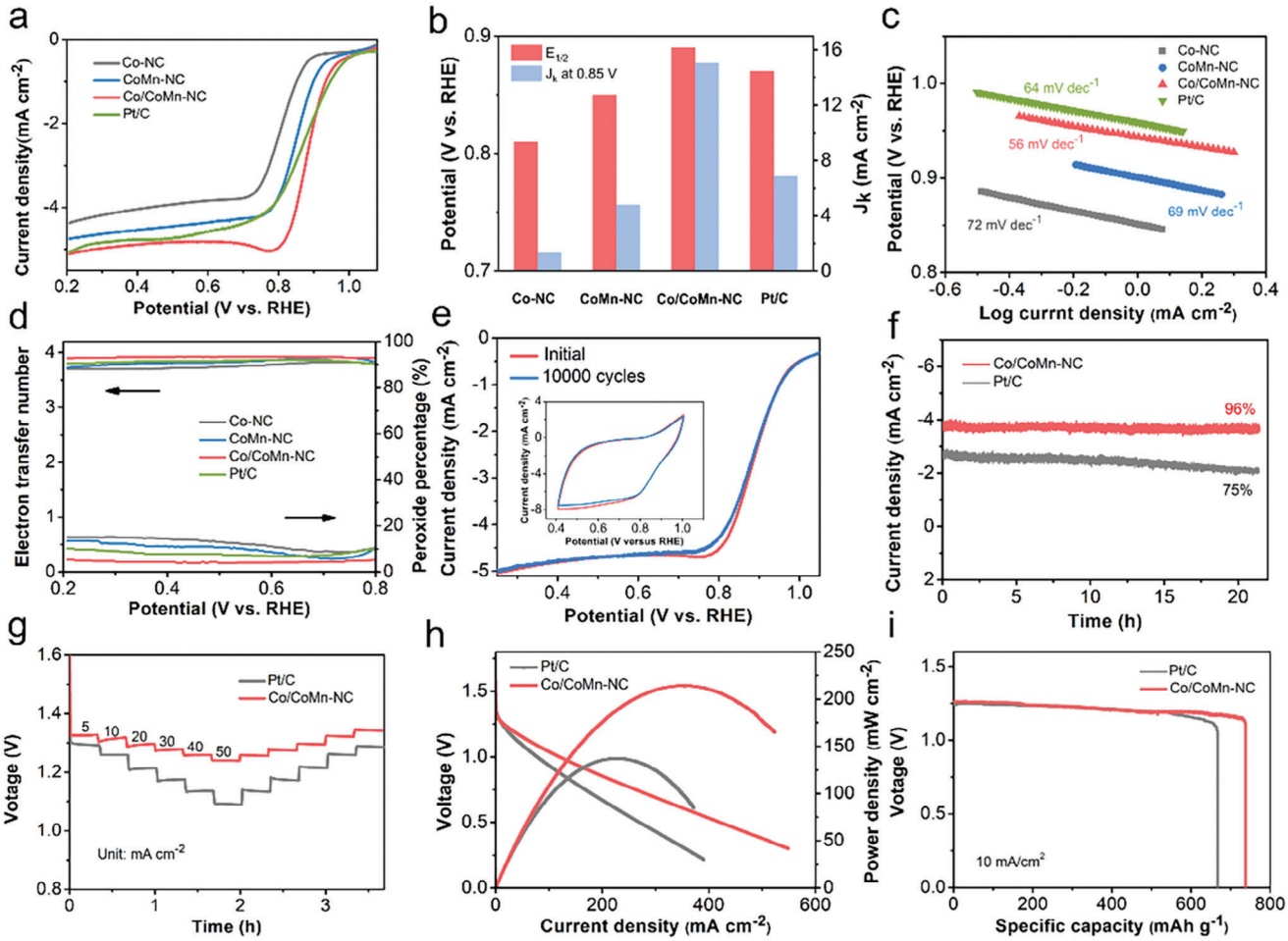

Figure 3. ORR performances and Zn–Air Batteries system utilizing Co/CoMn-NC catalysts. a) LSV curves in O_2-saturated 0.1 M KOH solution, b) comparison of $E_{1/2}$ and J_k, and c) Tafel plots of Co-NC, CoMn-NC, Co/CoMn-NC, and Pt/C catalysts. d) Electron transfer number (n) and H_2O_2 yield in 0.1 M KOH solution. e) ORR polarization curves and CV curves before and after 10 000 cycles for Co/CoMn-NC. f) Chronoamperometric tests of Co/CoMn-NC and Pt/C at 0.85 V versus RHE. g) Discharge curves at different current densities of Co/CoMn-NC. h) Polarization and power density curves of the primary Zn–air batteries of Co/CoMn-NC and Pt/C. i) Specific capacity of the Zn–air battery for Co/CoMn-NC and Pt/C.

supported by the Koutecky–Levich (K–L) determination, which was obtained from the polarization curves of Co/CoMn-NC at different rotating speeds (Figure S19, Supporting Information). Furthermore, the electrochemically active surface areas (ECSAs) were estimated by the electric double-layer capacitance method (Figure S20, Supporting Information) to evaluate the intrinsic activity of Co/CoMn-NC. Electrochemical double-layer capacitances (C_{dl}) of 19.9, 27.7, and 43.3 mF cm^{-2}, recorded for Co-NC, CoMn-NC, and Co/CoMn-NC respectively, underscore the enhanced capabilities of Co/CoMn-NC in revealing more active sites and achieving higher atomic utilization for oxygen adsorption and subsequent reactions. Moreover, electrochemical impedance spectroscopy (EIS) reveals that the charge transfer resistance during the ORR on Co/CoMn-NC is the smallest compared to other samples (Figure S21, Supporting Information), further confirmed the substantially enhanced ORR activity of Co/CoMn-NC. In addition to the high catalytic activity, Co/CoMn-NC also demonstrates outstanding durability, exhibiting a degradation of merely 5 mV in $E_{1/2}$ after 10 000 potential cycles in O_2-saturated 0.1 M KOH solution (Figure 3e). The chronoamperometry test (Figure 3f) further confirms the outstanding stability. Co/CoMn-NC maintains 96% of its initial current density after a 20-hour continues testing, surpassing that of Pt/C (75%).

Inspired by the excellent ORR catalytic capability, we further employed Co/CoMn-NC catalyst as the air cathode to assemble a primary Zn–air battery to show the viability of Co/CoMn-NC in the practical application of energy conversion devices. The Co/CoMn-NC-based battery shows a high open-circuit voltage (OCV) of 1.45 V, which is larger than that of the Pt/C (1.39 V) (Figure S22, Supporting Information). The discharge curves of the Zn–air batteries showing in Figure 3g demonstrate Co/CoMn-NC-based battery can deliver stable discharge potentials at different currents, thereby revealing the excellent ORR stability and reversibility. Discharging polarization curves and corresponding power density of catalysts were plotted in Figure 3h and the Co/CoMn-NC unfolds a higher maximum power density of 213 mW cm^{-2}, superior to that of commercial Pt/C based battery (136 mW cm^{-2}). Furthermore, the specific capacity of the Co/CoMn-NC-based battery was calculated to be 735.8 $mAhg^{-1}$, exceeding the Pt/C-based battery (519.2 $mAhg^{-1}$) (Figure 3i).

© 2024 Wiley-VCH GmbH

16163028, 0, Downloaded from https://onlinelibrary.wiley.com/doi/10.1002/adfm.202315862 by National University Of Singapore Nus Libraries, Wiley Online Library on [24/04/2024]. See the Terms and Conditions (https://onlinelibrary.wiley.com/terms-and-conditions) on Wiley Online Library for rules of use; OA articles are governed by the applicable Creative Commons License

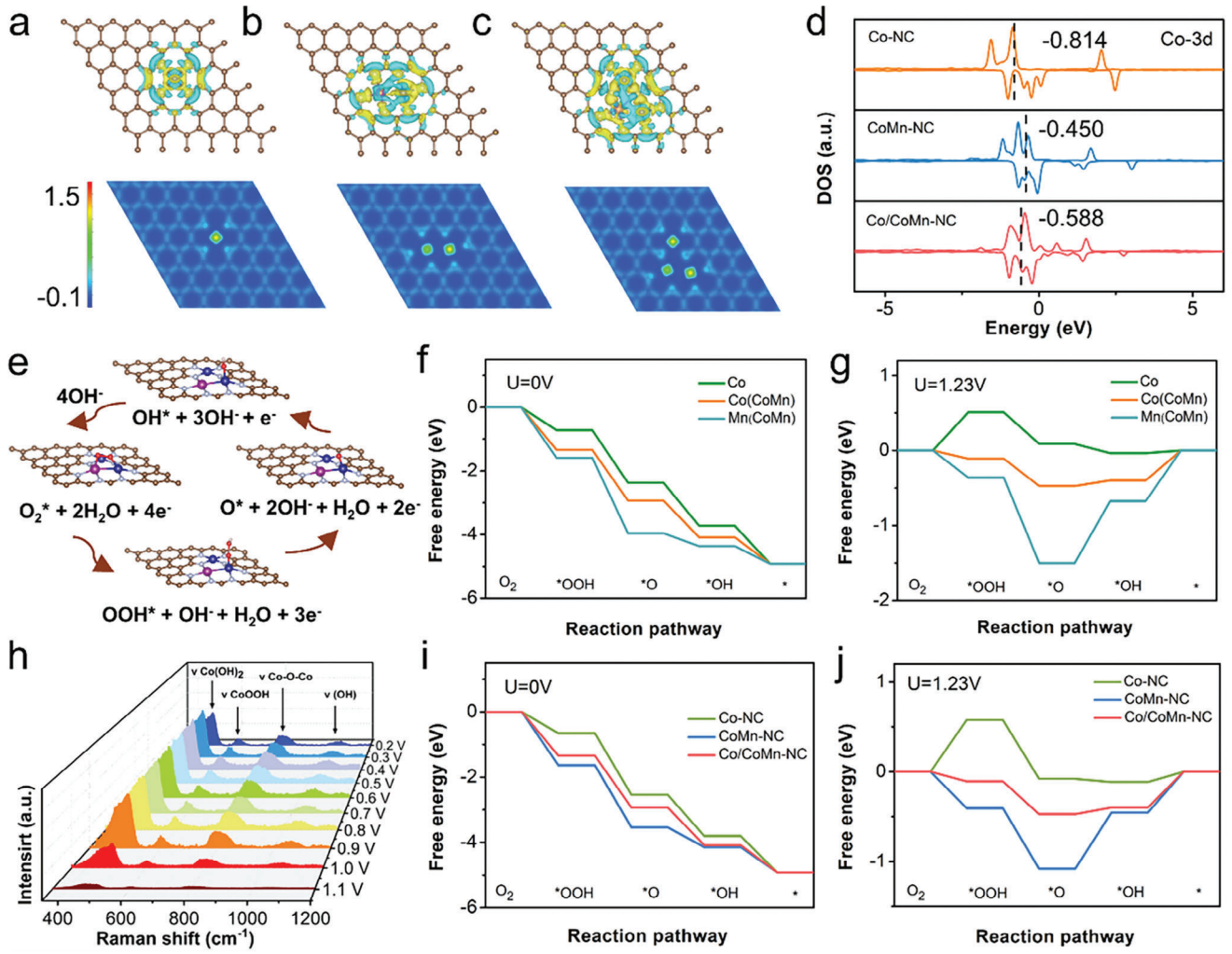

Figure 4. DFT calculations of the ORR activity on Co/CoMn-NC catalysts. Calculated charge density differences for a) Co-NC, b) CoMn-NC, and c) Co/CoMn-NC. d) DOS of Co-NC, CoMn-NC, and Co/CoMn-NC. e) Proposed ORR elemental steps for Co/CoMn-NC. Free energy diagram for ORR process on the three active sites of Co/CoMn-NC at f) U = 0 V and g) U = 1.23 V. h) In situ Raman spectra of Co/CoMn-NC in 0.1 M KOH. Free energy diagram for ORR process on Co-NC, CoMn-NC, and Co/CoMn-NC at i) U = 0 V and j) U = 1.23 V.

The high performance exhibited by atomically dispersed catalysts is largely attributed to the microscopic electronic structure of the atomic-scale active sites in the catalysts. Therefore, it is crucial to deeply understand the relationship between macroscopic properties and microscopic electronic structure.[52,53] To further disclose the active-sites identity and the origin of the superior catalytic performance of Co/CoMn-NC for ORR, DFT calculations were performed to delve deeper into the catalytic mechanism. Owning to the diverse sites on Co/CoMn-NC, three structural models of Co-NC, CoMn-NC and Co/CoMn-NC on N-doped carbon were constructed and optimized (Figure S23, Supporting Information). Then, we computed the oxygen adsorption models on Co-NC, CoMn-NC, and Co/CoMn-NC, as shown in Figure S24 (Supporting Information). Specifically, we considered two adsorption modes for oxygen on the CoMn diatomic sites: Modul (1-CoMn) and Modul (2-CoMn). Then, the Gibbs free energy (ΔG) diagram was calculated to explore the impact of the synergy of Co single-atom sites and CoMn dual-atom sites on the ORR activity (Figure S25, Supporting Information). As a result, we obtained an O_2 adsorption energy of −0.45 eV in the Co-NC system. In contrast, the adsorption energies of O_2 for Modul (1-CoMn) and Modul (2-CoMn) were calculated to be −2.039 and −2.399 eV, respectively, in the CoMn-NC system. This result indicates that O_2 adsorption at the CoMn-NC site is mainly in the form of bridging sites (2-CoMn) and energetically more stable than that of Co-NC. Excessive oxygen adsorption energy indicates overly strong oxygen binding, potentially limiting proton-electron transfer (*O or *OH) in CoMn-NC, resulting in suboptimal ORR activity. In contrast, when oxygen is adsorbed by Co/CoMn-NC, it leads to appropriate O_2 adsorption energy and suitable binding energy. This is due to the synergy between Co single-atom sites and CoMn dual-atom sites, which reduces the O_2 dissociation energy barrier.

The polarized charge densities of the three models are shown in **Figure** 4a–c. It's noticeable that the electron density of the Co site in CoMn-NC increases compared to Co-NC. This suggests

© 2024 Wiley-VCH GmbH

16163028, 0, Downloaded from https://onlinelibrary.wiley.com/doi/10.1002/adfm.202315862 by National University Of Singapore Nus Libraries, Wiley Online Library on [24/04/2024]. See the Terms and Conditions (https://onlinelibrary.wiley.com/terms-and-conditions) on Wiley Online Library for rules of use; OA articles are governed by the applicable Creative Commons License

that electron transfer from the Mn site to the Co site occurs due to the difference in their electronegativity, which aligns with the XANES results discussed earlier. Whereas, in the Co/CoMn-NC, the Co single atom transfers a part of electrons to the CoMn dual atom to optimize the electronic structure of the active site (Figure 4c). This is also confirmed by the results of the density of states calculations (Figures S26–S28, Supporting Information). Furthermore, Figure 4b shows substantial energy positive shift for d-band center of Co in CoMn-NC compared to Co-NC (from −0.814 to −0.450 eV). Additionally, the moderate d-band center of Co (−0.588 eV) in Co/CoMn-NC, when compared to the Co-NC and CoMn-NC, indicates that Co/CoMn-NC possesses the optimal adsorption energy for ORR intermediates.

In the case of Co/CoMn-NC, potential active sites include Co single atoms, Mn sites within CoMn dual-atom configurations, and Co sites within CoMn dual-atom configurations. To further confirm the electrocatalytic active center, the adsorption models of *OOH, *O, and *OH species, and the ORR processes on three different sites in Co/CoMn-NC models are computed and depicted in Figures S29 and S30 (Supporting Information) and Figure 4e. The ORR processes on these three sites for Co/CoMn-NC were calculated at U = 0 V versus RHE and the equilibrium potential U = 1.23 V versus RHE, respectively. As illustrated in Figure 4f, at U = 0 V, all the reaction steps from O_2 to OH^- are downhill, suggesting a spontaneous reaction. In contrast, several endothermic ORR pathways occur (Figure 4g) at U = 1.23 V. The first ORR step ($* + O_2 + H_2O + e^- \rightarrow {}^*OOH + OH^-$) for the Co single atom is uphill and considered endergonic, implying sluggish oxygen adsorption and *OOH formation. The Mn site of the CoMn dual-atom site exhibits the steepest uphill energy barrier at the elementary step of $^*O + e^- + H_2O = {}^*OH + OH^-$, indicating extremely slow kinetics for ORR on the Mn active site. In contrast, the Co site within the CoMn dual-atom configuration displays the smallest energy difference among *OOH, *O, and *OH, suggesting that it is likely the primary active site for ORR within Co/CoMn-NC.[54–56]

To verify the catalytic mechanism proposed for Co/CoMn-NC, we carried out in situ Raman spectroscopy to monitor the reaction intermediates, as well as identify potential active sites during ORR. As shown in Figure 4h, in the initial state, no obvious peaks were observed, indicating that the ORR process did not occur. As the cathodic potential decreases, two peaks appear at 500 and 605 cm^{-1}, attributed to $Co(OH)_2$ and CoOOH, respectively.[57] In addition, the new peaks observed at 802 and 1048 cm^{-1} can be attributed to the characteristic peaks for Co–O–Co vibration and OH deformation mode, respectively.[58] Importantly, no other peaks related to Mn species were observed, indicating that Mn site is unlikely the active center in the Co/CoMn-NC catalyst. The Gibbs free energy diagrams of ORR on Co-NC, CoMn-NC and Co/CoMn-NC are computed and depicted in Figure 4i,j. When U = 0 V, all electron transfer steps for all the above three models pose a consistent spontaneous exothermal process. Notably, upon increasing the potential to 1.23 V, Co/CoMn-NC has the lowest energy barrier and the optimal free-energy path, thereby optimizing the adsorption and dissociation of the oxygenated intermediate and facilitating four-electron oxygen reduction. The rate-determining-step (RDS) is desorption of OH^*, which has also been verified by in situ Raman.

3. Conclusion

In summary, we have developed a systematic strategy to understand catalyst materials with various atomically dispersed active sites. We introduced a novel structural model, Co/CoMn-NC, combining Co single-atom and CoMn dual-atom sites on N-doped carbon. This synergy resulted in excellent ORR performance in alkaline media ($E_{1/2}$ = 0.89 V in 0.1 M KOH) and outstanding Zn–air battery performance (213 mW cm^{-2} at 401 mA cm^{-2}). Our approach involved X-ray absorption spectroscopy and DFT calculations to determine the precise atomic structure. Detailed investigations and theoretical calculations revealed that the synergy between Co single-atom and CoMn dual-atom sites effectively adjusted the d-band center of the active sites, reducing the energy barrier for 4e- ORR. Our work challenges conventional understanding of atomically dispersed multi-metal-nitrogen-carbon catalysts and provides deeper insights for future cost-effective and efficient catalyst design.

Supporting Information

Supporting Information is available from the Wiley Online Library or from the author.

Acknowledgements

This work was financially supported by the National Natural Science Foundation of China (No. 52122107 and 51972224). L. Wang would like to acknowledge the support of the National Research Foundation (NRF) Singapore, under the NRF Fellowship (NRF-NRFF13-2021-0007), as well as the support from the Centre for Hydrogen Innovations at the NUS (CHI-P2022-06).

Conflict of Interest

The authors declare no conflict of interest.

Data Availability Statement

The data that support the findings of this study are available from the corresponding author upon reasonable request.

Keywords

atomically dispersed multi-metal-nitrogen-carbon catalysts, the atomic configuration, in situ Raman, oxygen reduction reaction

Received: January 10, 2024
Published online:

[1] J. Yang, W. Li, D. Wang, Y. Li, *Adv. Mater.* **2020**, *32*, 22003300.
[2] Y. Xiong, J. Dong, Z. Huang, P. Xin, W. Chen, Y. Wang, Z. Li, Z. Jin, W. Xing, Z. Zhuang, J. Ye, X. Wei, R. Cao, L. Gu, S. Sun, L. Zhuang, X. Chen, H. Yang, C. Chen, Q. Peng, C. Chang, D. Wang, Y. Li, *Nat. Nanotechnol.* **2020**, *15*, 390.
[3] J. Li, H. Zhang, W. Samarakoon, W. Shan, D. A. Cullen, S. Karakalos, M. Chen, D. Gu, K. L. More, G. Wang, Z. Feng, Z. Wang, G. Wu, *Angew. Chem., Int. Ed.* **2019**, *5*, 18971.

© 2024 Wiley-VCH GmbH

16163028, 0, Downloaded from https://onlinelibrary.wiley.com/doi/10.1002/adfm.202315862 by National University Of Singapore Nus Libraries, Wiley Online Library on [24/04/2024]. See the Terms and Conditions (https://onlinelibrary.wiley.com/terms-and-conditions) on Wiley Online Library for rules of use; OA articles are governed by the applicable Creative Commons License

[4] J. Sui, H. Liu, S. Hu, K. Sun, G. Wang, H. Zhou, X. Zheng, H.-L. Jiang, *Adv. Mater.* **2022**, *34*, 21109203.
[5] Z. Chen, S. Wu, J. Ma, S. Mine, T. Toyao, M. Matsuoka, L. Wang, J. Zhang, *Angew. Chem., Int. Ed.* **2021**, *60*, 11901.
[6] P. Zhou, Q. Zhang, Z. Xu, Q. Shang, L. Wang, Y. Chao, Y. Li, H. Chen, F. Lv, Q. Zhang, L. Gu, S. Guo, *Adv. Mater.* **2020**, *32*, 1904249.
[7] J. Sun, H. Jiang, P. Dixneuf, M. Zhang, *J. Am. Chem. Soc.* **2023**, *145*, 17329.
[8] H. Qi, J. Yang, F. Liu, L. Zhang, J. Yang, X. Liu, L. Li, Y. Su, Y. Liu, R. Hao, A. Wang, T. Zhang, *Nat. Commun.* **2021**, *12*, 3295.
[9] W. Liu, L. Zhang, W. Yan, X. Liu, X. Yang, S. Miao, W. Wang, A. Wang, T. Zhang, *Chem. Sci.* **2016**, *7*, 5758.
[10] J. Xi, H. Jung, Y. Xu, F. Xiao, J. Bae, S. Wang, *Adv. Funct. Mater.* **2021**, *31*, 2008318.
[11] Y. Chen, S. Ji, C. Chen, Q. Peng, D. Wang, Y. Li, *Joule* **2018**, *2*, 1242.
[12] H. Fei, J. Dong, Y. Feng, C. Allen, C. Wan, B. Volosskiy, M. Li, Z. Zhao, Y. Wang, H. Sun, P. An, W. Chen, Z. Guo, C. Lee, D. Chen, I. Shakir, M. Liu, T. Hu, Y. Li, A. Kirkland, X. Duan, Y. Huang, *Nat. Catal.* **2018**, *1*, 63.
[13] N. Cheng, L. Zhang, K. Doyle-Davis, X. Sun, *Electrochem. Energy Rev.* **2019**, *2*, 539.
[14] J. Xi, H. Jung, Y. Xu, F. Xiao, J. Bae, S. Wang, *Adv. Funct. Mater.* **2020**, *31*, 2008318.
[15] A. Wang, J. Li, T. Zhang, *Nat. Rev. Chem.* **2018**, *2*, 65.
[16] G. Sun, Z. Zhao, R. Mu, S. Zha, L. Li, S. Chen, K. Zang, J. Luo, Z. Li, S. Purdy, A. Kropf, J. Miller, L. Zeng, J. Gong, *Nat. Commun.* **2018**, *9*, 4454.
[17] X. Wan, X. Liu, Y. Li, R. Yu, L. Zheng, W. Yan, H. Wang, M. Xu, J. Shui, *Nat. Catal.* **2019**, *2*, 259.
[18] J. Pampel, T.-P. Fellinger, *Adv. Energy Mater.* **2016**, *6*, 150238.
[19] H. Zhang, G. Liu, L. Shi, J. Ye, *Adv. Energy Mater.* **2018**, *8*, 1701343.
[20] D. Kunwar, S. Zhou, A. DeLaRiva, E. Peterson, H. Xiong, X. Pereira-Hernández, S. Purdy, R. t. Veen, H. Brongersma, J. Miller, H. Hashiguchi, L. Kovarik, S. Lin, H. Guo, Y. Wang, A. Datye, *ACS Catal.* **2019**, *9*, 3978.
[21] A. Sarapuu, E. Kibena-Põldsepp, M. Borghei, K. Tammeveski, *J. Mater. Chem. A* **2018**, *6*, 776.
[22] Z. Lu, B. Wang, Y. Hu, W. Liu, Y. Zhao, R. Yang, Z. Li, J. Luo, B. Chi, Z. Jiang, M. Li, S. Mu, S. Liao, J. Zhang, X. Sun, *Angew. Chem., Int. Ed.* **2019**, *58*, 2622.
[23] W. Zhang, Y. Chao, W. Zhang, J. Zhou, F. Lv, K. Wang, F. Lin, H. Luo, J. Li, M. Tong, E. Wang, S. Guo, *Adv. Mater.* **2021**, *33*, 2102576.
[24] H. Yang, T. Zhang, X. Chi, X. Yu, J. Chen, J. Chen, C. Li, S. Tan, Q. He, X. Wang, L. Wang, *J. Mater. Chem. A* **2022**, *10*, 19626.
[25] Y. Zang, D. Lu, K. Wang, B. Li, P. Peng, Y. Lan, S. Zang, *Nat. Commun.* **2023**, *14*, 1792.
[26] X. Han, X. Ling, D. Yu, D. Xie, L. Li, S. Peng, C. Zhong, N. Zhao, Y. Deng, W. Hu, *Adv. Mater.* **2019**, *31*, 1905622.
[27] Y. Chen, S. Hu, F. Nichols, F. Bridges, S. Kan, T. He, Y. Zhang, S. Chen, *J. Mater. Chem. A* **2020**, *8*, 11649.
[28] M. Xiao, Y. Chen, J. Zhu, H. Zhang, X. Zhao, L. Gao, X. Wang, J. Zhao, J. Ge, Z. Jiang, S. Chen, C. Liu, W. Xing, *J. Am. Chem. Soc.* **2019**, *141*, 17763.
[29] A. Kumar, V. Bui, J. Lee, L. Wang, A. Jadhav, X. Liu, X. Shao, Y. Liu, J. Yu, Y. Hwang, H. Bui, S. Ajmal, M. Kim, S. Kim, G. Park, Y. Kawazoe, H. Lee, *Nat. Commun.* **2021**, *12*, 6766.
[30] J. Ding, F. Li, J. Zhang, Q. Zhang, Y. Liu, W. Wang, W. Liu, B. Wang, J. Cai, X. Su, H. Yang, X. Yang, Y. Huang, Y. Zhai, B. Liu, *J. Am. Chem. Soc.* **2023**, *145*, 11829.
[31] F. Huang, M. Peng, Y. Chen, X. Cai, X. Qin, N. Wang, D. Xiao, L. Jin, G. Wang, X.-D. Wen, H. Liu, D. Ma, *J. Am. Chem. Soc.* **2022**, *144*, 18485.
[32] T. Gu, D. Zhang, Y. Yang, C. Peng, D. Xue, C. Zhi, M. Zhu, J. Liu, *Adv. Funct. Mater.* **2022**, *33*, 2212299.
[33] Z. Jiang, X. Liu, X. Liu, S. Huang, Y. Liu, Z. Yao, Y. Zhang, Q. Zhang, L. Gu, L. Zheng, L. Li, J. Zhang, Y. Fan, T. Tang, Z. Zhuang, J. Hu, *Nat. Commun.* **2023**, *14*, 1822.
[34] S. Gong, C. Wang, P. Jiang, L. Hu, H. Lei, Q. Chen, *J. Mater. Chem. A* **2018**, *6*, 13254.
[35] W. Ren, X. Tan, W. Yang, C. Jia, S. Xu, K. Wang, S. Smith, C. Zhao, *Angew. Chem., Int. Ed.* **2019**, *58*, 6972.
[36] Y. Li, B. Wei, M. Zhu, J. Chen, Q. Jiang, B. Yang, Y. Hou, L. Lei, Z. Li, R. Zhang, Y. Lu, *Adv. Mater.* **2021**, *33*, 2102212.
[37] Z. Zhang, C. Feng, C. Liu, M. Zuo, L. Qin, X. Yan, Y. Xing, H. Li, R. Si, S. Zhou, J. Zeng, *Nat. Commun.* **2020**, *11*, 1215.
[38] X. Li, W. Bi, L. Zhang, S. Tao, W. Chu, Q. Zhang, Y. Luo, C. Wu, Y. Xie, *Adv. Mater.* **2016**, *28*, 2427.
[39] J. Li, M. Chen, D. Cullen, S. Hwang, M. Wang, B. Li, K. Liu, S. Karakalos, M. Lucero, H. Zhang, C. Lei, H. Xu, *Nat. Catal.* **2018**, *1*, 935.
[40] X. Yan, D. Liu, P. Guo, Y. He, X. Wang, Z. Li, H. Pan, D. Sun, F. Fang, R. Wu, *Adv. Mater.* **2023**, *35*, 2210975.
[41] Y. Pan, S. Liu, K. Sun, X. Chen, B. Wang, K. Wu, X. Cao, W. Cheong, R. Shen, A. Han, Z. Chen, L. Zheng, J. Luo, Y. Lin, Y. Liu, D. Wang, Q. Peng, Q. Zhang, C. Chen, Y. Li, *Angew. Chem., Int. Ed.* **2018**, *57*, 8614.
[42] M. Qiao, Y. Wang, T. Wågberg, X. Mamat, X. Hu, G. Zou, G. Hu, *J. Energy Chem.* **2020**, *47*, 146.
[43] T. Wang, X. Cao, H. Qin, L. Shang, S. Zheng, F. Fang, L. Jiao, *Angew. Chem., Int. Ed.* **2021**, *60*, 21237.
[44] J. Wang, Z. Huang, W. Liu, C. Chang, H. Tang, Z. Li, W. Chen, C. Jia, T. Yao, S. Wei, Y. Wu, Y. Li, *J. Am. Chem. Soc.* **2017**, *139*, 17281.
[45] S. Sarkar, A. Biswas, T. Purkait, M. Das, N. Kamboj, R. Dey, *Inorg. Chem.* **2020**, *59*, 5194.
[46] M. Tong, F. Sun, Y. Xie, Y. Wang, Y. Yang, C. Tian, L. Wang, H. Fu, *Angew. Chem., Int. Ed.* **2021**, *60*, 14005.
[47] G. Yang, J. Zhu, P. Yuan, Y. Hu, G. Qu, B. Lu, X. Xue, H. Yin, W. Cheng, J. Cheng, W. Xu, J. Li, J. Hu, S. Mu, J. Zhang, *Nat. Commun.* **2021**, *12*, 1734.
[48] X. Zhu, D. Zhang, C.-J. Chen, Q. Zhang, R.-S. Liu, Z. Xia, L. Dai, R. Amal, X. Lu, *Nano Energy* **2020**, *71*, 104597.
[49] J. Xue, Y. Li, J. Hu, *J. Mater. Chem. A* **2020**, *8*, 7145.
[50] A. Holewinski, S. Linic, *J. Electrochem. Soc.* **2012**, *159*, H864.
[51] T. Shinagawa, A. Garcia-Esparza, K. Takanabe, *Sci. Rep.* **2015**, *5*, 13801.
[52] R. Li, J. Zhao, B. Liu, D. Wang, P. Kuang, Z. Ni, B. Zhu, Y. Lin, J. Yu, *Adv. Mater.* **2023**, *36*, 2308653.
[53] J. Yang, W. Li, D. Wang, Y. Li, *Small Struct.* **2021**, *2*, 2000051.
[54] P. Kuang, Z. Ni, B. Zhu, Y. Lin, J. Yu, *Adv. Mater.* **2023**, *35*, 2303030.
[55] X. Wu, Q. Wang, S. Yang, J. Zhang, Y. Cheng, H. Tang, L. Ma, X. Min, C. Tang, S. Jiang, F. Wu, Y. Lei, S. Ciampic, S. Wang, L. Dai, *Energy Environ. Sci.* **2022**, *15*, 1183.
[56] L. Wang, W. Tian, W. Zhang, F. Yu, Z. Yuan, *Appl. Catal. B-Environ.* **2023**, *338*, 123043.
[57] M. Li, H. Zhu, Q. Yuan, T. Li, M. Wang, P. Zhang, Y. Zhao, D. Qin, W. Guo, B. Liu, X. Yang, Y. Liu, Y. Pan, *Adv. Funct. Mater.* **2023**, *33*, 221086.
[58] M. Jiang, F. Wang, F. Yang, H. He, J. Yang, W. Zhang, J. Luo, J. Zhang, C. Fu, *Nano Energy* **2022**, *93*, 106793.

© 2024 Wiley-VCH GmbH

16163028, 0, Downloaded from https://onlinelibrary.wiley.com/doi/10.1002/adfm.202315862 by National University Of Singapore Nus Libraries, Wiley Online Library on [24/04/2024]. See the Terms and Conditions (https://onlinelibrary.wiley.com/terms-and-conditions) on Wiley Online Library for rules of use; OA articles are governed by the applicable Creative Commons License